Int. J. Heat Mass Transfer. Vol. 35, No. 10, pp. 2537–2550, 1992
Printed in Great Britain

0017–9310/92 $5.00 + 0.00

Convective heat transfer in the developing flow region of a square duct with strong curvature

JAE HWA CHUNG and JAE MIN HYUN†
Department of Mechanical Engineering, Korea Advanced Institute of Science and Technology, P.O. Box 150, Cheong Ryang, Seoul, Korea

(*Received* 11 *March* 1991 *and in final form* 4 *September* 1991)

Abstract—A comprehensive numerical study is made of the velocity and convective heat transfer characteristics of developing laminar flow in a 90° curved square duct. Straight inlet and outlet tangents are attached to the duct. The fully elliptic, three-dimensional, steady, incompressible Navier–Stokes equations are solved numerically over wide ranges of Reynolds number *Re* (and corresponding Dean number). A body-fitted coordinate system is utilized. Two thermal boundary conditions at the bend were adopted: a constant wall temperature condition, and a constant wall heat flux condition. The elaborate numerical results are consistent with the available flow field data. The details of the temperature field as well as the Nusselt number in the curved region are depicted. The influence of *Re* on local heat transfer in various parts of flow field is scrutinized. The impact of the thermal boundary condition at the bend is examined. In the vicinity of the entrance of the curved region, heat transfer is higher on the inner wall due to the presence of local accelerating flows near the inner wall. However, at further downstream, heat transfer is higher on the outer wall, since the maximum of the mainstream is shifted toward the outer and side walls by the action of centrifugal force. As the Reynolds number increases, a region of reverse flow appears in the corner area between the outer and side walls near the inlet of the bend. Heat transfer is reduced in this region of reverse flow. The present computational results clearly illustrate the variations of the Nusselt numbers, both in the peripheral and streamwise directions.

1. INTRODUCTION

CONSIDERABLE interest has recently been shown in three-dimensional flow and heat transfer characteristics of fluids passing through a strongly curved duct. This has been motivated by the need to acquire an improved understanding of transport processes at work. Strongly curved ducts, in particular, with square cross-section, are widely used in various types of heat-exchanging industrial devices and high-tech electronic systems. One prominent feature is the generation of the secondary flow, which mainly results from the dynamic interplays of pressure gradient, centrifugal force and viscous effects. Owing to these secondary flows, convective transports are generally more effective in a curved duct than in a straight duct of comparable size. However, substantial local variations of heat transfer are also noted in a curved duct. This warrants a thorough examination of the flow and heat transfer properties, local as well as global, in order to design and operate efficiently these sophisticated modern technological systems.

The importance of accurate analyses of three-dimensional flow fields in a curved duct has well been recognized; however, comprehensive and validated information on heat transfer characteristics under developing flow conditions has been relatively scanty. Most of the existing flow data have been obtained for fully developed flows [1, 2]. The primary concern of these investigations has been with the structure of secondary flow. Reference [3] presented experimental data on the velocity distributions for developing flows in a 90° curved square duct by using a laser Doppler velocimeter. A parallel computation was also made in ref. [3] by use of a rather coarse grid network. Complementary flow field measurements were reported later by ref. [4].

Prior studies available in the literature on heat transfer in a curved duct mostly dealt with the cases of fully-developed heat transfer under fully-developed flow conditions [5, 6] or developing heat transfer under fully-developed flow conditions [7]. Only a few experimental investigations on developing heat transfer in developing curved duct flow were documented, and they were in the turbulent flow regime, e.g. ref. [8]. The scarcity of reliable heat transfer data in developing flows in a curved duct is conspicuous in the engineering literature.

Numerical simulations of developing curved duct flows and associated heat transfer have been a formidable undertaking. Extreme complexities are involved in computing three-dimensional flows over broad ranges of relevant parameters. Consequently, preceding numerical efforts were carried out under restrictive and simplifying assumptions in solving the governing Navier–Stokes equations [9, 10]. However, the deficiencies and potentially erroneous results

† Author to whom correspondence should be addressed.

NOMENCLATURE

A^u link coefficient for the u-momentum equation
A^v link coefficient for the v-momentum equation
A^w link coefficient for the w-momentum equation
C_p pressure coefficient $((P^* - P_0)/(\rho u_0^2/2))$
$\bar{C}_p$ average pressure coefficient over the duct cross-section
$\bar{C}_{p_w}$ average pressure coefficient at the duct wall
D hydraulic diameter of the duct
De Dean number $(Re(D/2r_0)^{1/2})$
L width of wall
L_p peripheral length of the duct
n normal direction to the wall
Nu local Nusselt number at the wall (hD/κ)
Nu plane-averaged Nusselt number at the wall
Nu_p peripherally-averaged Nusselt number at the wall
P nondimensional pressure
P^* dimensional pressure
$\hat{P}$ guessed pressure
P' correction pressure
P_0 dimensional duct inlet pressure
Pr Prandtl number (ν/α)
q heat flux
R curvature ratio (r_0/D)
r_0 dimensional mean radius of the curved region
Re Reynolds number $(u_0 D/\nu)$
S_c dimensional total surface area of the curved region of the duct
S^ϕ source term for the general scalar ϕ
S^u source term for the u-momentum equation
S^v source term for the v-momentum equation
S^w source term for the w-momentum equation
T nondimensional temperature
T^* dimensional temperature
T_b nondimensional bulk temperature
T_0 dimensional duct inlet temperature
T_w dimensional wall temperature
u_0 dimensional average velocity at the duct inlet
u, v, w nondimensional velocity components
u^*, v^*, w^* dimensional velocity components
$\hat{u}, \hat{v}, \hat{w}$ guessed velocity components
u', v', w' correction velocity components
U, V, W contravariant velocity components
x, y, z nondimensional cartesian coordinates
x^*, y^*, z^* dimensional cartesian coordinates.

Greek symbols
α thermal diffusivity
Γ^ϕ effective diffusion coefficient
θ curve angle
κ thermal conductivity of the fluid
ν kinematic viscosity
ξ, η, ζ curvilinear coordinates
ρ density
ϕ dependent variable of general transport equation.

obtained by using simplified versions of the governing equations, such as parabolic or semi-parabolic treatments, for duct flows with strong curvature have been explored [11]. Recently, publications illuminating the computational results of flow field at selected Reynolds numbers, secured by using elliptic three-dimensional formulations, indicated generally satisfactory agreement with the flow measurements [11, 12]. These previous endeavors substantially enlarged our rudimentary knowledge of global characteristics of flow and heat transfer in strongly-curved ducts.

The purpose of the present study is to provide an enhanced understanding of local heat transfer properties in the developing region of a curved duct. The subject is of particular importance at higher Reynolds numbers and with stronger curvature; the possibility of the existence of reversed flow regions near the inlet of the curved section leads to a significant reduction of local convective heat transfer in these zones. The main thrust of the present work is placed on carrying out extensive and in-depth numerical calculations of developing convective flow and heat transfer over a wide range of Reynolds numbers. The unapproximated, elliptic, three-dimensional steady incompressible Navier–Stokes equations are solved numerically. The computational results will provide a valuable check to verify the previous numerical predictions which were obtained under several restrictive approximations, such as parabolic or semi-parabolic formulations.

In the present paper, it is intended to extend the numerical simulations in a systematic way to disclose the explicit dependence of the results on the Reynolds number. The local thermal field data in the developing flow region have not been given in sufficient detail in the literature. References [11], [13] illustrated numerical results for one value of the Reynolds number using a constant wall temperature boundary con-

dition at the bend. One objective of the present study is to comprehend the change in flow character under two different thermal boundary conditions, i.e. a constant wall temperature condition and a constant wall heat flux condition. Owing to the greatly expanded computing resources, the computational mesh network is appreciably finer in the present paper than those of the preceding numerical studies [11, 13]. It is also worth mentioning that the temperature field data of ref. [11] were acquired with the inlet and outlet tangents excluded. This may introduce some unspecified numerical errors. It is of interest to point out another potentially significant improvement in numerical computational methodology of the present study. In the prior investigations [3, 11, 13], three different coordinate systems were used to handle separately the straight ducts and the bend region. However, as observed by Kajishima *et al.* [14], such numerical procedures may produce numerical errors due to the discontinuity at the conjunction zones of two different adjoining coordinate systems. In an effort to remedy such possible localized numerical inconsistencies, a continuous body-fitted coordinate system is utilized in the present study. These will presumably increase the accuracy and reliability of the present numerical results.

The numerical results are processed to describe the three-dimensional features of flow and heat transfer inside of and on the duct wall in the developing flow region. The principal dynamic ingredients peculiar to developing three-dimensional flow and heat transfer will be identified and plausible explanations will be rendered. Emphasis is given to the axial variations of the average Nusselt number as well as to the peripheral variations of the local Nusselt number on the curved duct wall. These issues have not been explicitly addressed in the earlier investigations.

In connections with the presence of reversed flow zones, the necessity of using the elliptic formulation is stressed. The present study is supportive of the assertion that, at high Reynolds numbers, a reversed flow zone appears in the corner of the outer and side walls near the inlet of the curved region [3]; the associated heat transfer decreases measurably in this zone. When the thermal boundary condition is specified by a constant wall heat flux, the numerical results indicate substantial changes in local temperature in this corner area.

2. THE PROBLEM FORMULATION

The governing Navier–Stokes equations, expressed in nondimensionalized tensor form, are:

$$\frac{\partial}{\partial x_j}(u_j) = 0 \tag{1a}$$

$$\frac{\partial}{\partial x_j}(u_j u_i) = \frac{\partial P}{\partial x_i} + \frac{1}{Re}\frac{\partial}{\partial x_j}\left(\frac{\partial u_i}{\partial x_j}\right) \tag{1b}$$

$$\frac{\partial}{\partial x_j}(u_j T) = \frac{1}{Re\,Pr}\frac{\partial}{\partial x_j}\left(\frac{\partial T}{\partial x_j}\right) \tag{1c}$$

where $i, j = 1, 2, 3$,

$$Re = u_0 D/\nu, \quad Pr = \nu/\alpha.$$

In the above equations, (u_1, u_2 and u_3) are the velocity components in the x, y and z directions (expressed later as u, v and w, respectively); u_0 the dimensional average velocity at the duct entrance; D the hydraulic diameter of the duct; T the temperature; Pr the Prandtl number; Re the Reynolds number. In the present problem formulation, all the physical properties are taken to be constant.

The nondimensionalization is based on the following reference values for the respective dimensional physical quantities (starred):

$$x = x^*/D, \quad y = y^*/D, \quad z = z^*/D, \quad u = u^*/u_0,$$
$$v = v^*/u_0, \quad w = w^*/u_0, \quad P = P^*/(\rho u_0^2), \tag{2}$$

$$T = (T^* - T_0)/(T_w - T_0)$$

(in the case of constant wall temperature condition), (3a)

or

$$T = (T^* - T_0)/(q_w D/\kappa)$$

(in the case of constant wall heat flux condition) (3b)

where T_0 the dimensional duct inlet temperature, T_w the dimensional wall temperature in the curved region for the case of (3a), q_w the dimensional wall heat flux in the curved region, and κ the thermal conductivity of the fluid. Figure 1 shows a schematic of flow configuration.

Equations (1b) and (1c) can be written in terms

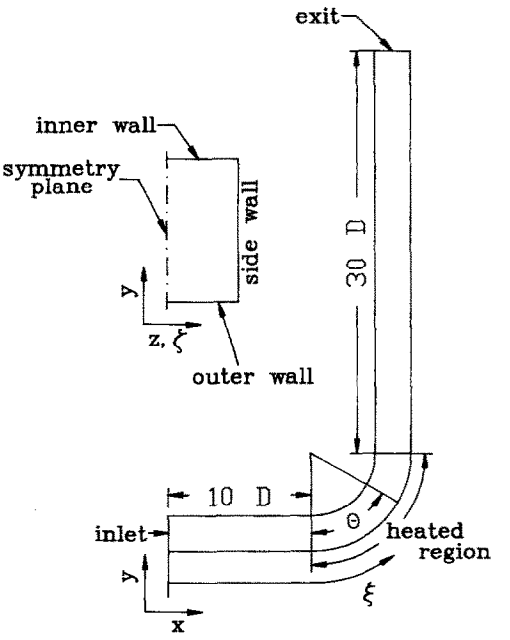

FIG. 1. Duct geometry and coordinate system.

of a single general equation for an arbitrary scalar dependent variable ϕ as

$$\frac{\partial}{\partial x_j}(u_j\phi) = \frac{\partial}{\partial x_j}\left(\Gamma^\phi \frac{\partial \phi}{\partial x_j}\right) + S^\phi \quad (4)$$

where Γ^ϕ is the effective diffusion coefficient, and S^ϕ the source term.

A general three-dimensional curvilinear coordinate system is introduced in solving the full elliptic forms of the Navier–Stokes equation. Let (ξ, η, ζ) be defined as

$$\xi = \xi(x, y, z), \quad \eta = \eta(x, y, z), \quad \zeta = \zeta(x, y, z), \quad (5)$$

then, equation (4) is transformed into

$$(U\phi)_\xi + (V\phi)_\eta + (W\phi)_\zeta = (\Gamma^\phi \alpha_1 \phi_\xi)_\xi + (\Gamma^\phi \alpha_2 \phi_\eta)_\eta + (\Gamma^\phi \alpha_3 \phi_\zeta)_\zeta + S \quad (6)$$

where,

$$U \equiv \xi_x u + \xi_y v + \xi_z w, \quad V \equiv \eta_x u + \eta_y v + \eta_z w,$$
$$W \equiv \zeta_x u + \zeta_y v + \zeta_z w,$$
$$S \equiv (\Gamma^\phi \beta_1 \phi_\eta)_\xi + (\Gamma^\phi \beta_3 \phi_\zeta)_\xi + (\Gamma^\phi \beta_1 \phi_\xi)_\eta + (\Gamma^\phi \beta_2 \phi_\zeta)_\eta + (\Gamma^\phi \beta_3 \phi_\xi)_\zeta + (\Gamma^\phi \beta_2 \phi_\eta)_\zeta + S^\phi$$

and

$$\alpha_1 \equiv (\xi_x^2 + \xi_y^2 + \xi_z^2), \quad \alpha_2 \equiv (\eta_x^2 + \eta_y^2 + \eta_z^2),$$
$$\alpha_3 \equiv (\zeta_x^2 + \zeta_y^2 + \zeta_z^2),$$
$$\beta_1 \equiv (\xi_x \eta_x + \xi_y \eta_y + \xi_z \eta_z),$$
$$\beta_2 \equiv (\eta_x \zeta_x + \eta_y \zeta_y + \eta_z \zeta_z),$$
$$\beta_3 \equiv (\zeta_x \xi_x + \zeta_y \xi_y + \zeta_z \xi_z)$$
$$\xi_x = J(y_\eta z_\zeta - y_\zeta z_\eta), \quad \xi_y = J(x_\zeta z_\eta - x_\eta z_\zeta),$$
$$\xi_z = J(x_\eta y_\zeta - x_\zeta y_\eta)$$
$$\eta_x = J(y_\zeta z_\xi - y_\xi z_\zeta), \quad \eta_y = J(x_\xi z_\zeta - x_\zeta z_\xi),$$
$$\eta_z = J(x_\zeta y_\xi - x_\xi y_\zeta)$$
$$\zeta_x = J(y_\xi z_\eta - y_\xi z_\eta), \quad \zeta_y = J(x_\eta z_\xi - x_\xi z_\zeta),$$
$$\zeta_z = J(x_\xi y_\eta - x_\eta y_\xi)$$
$$J = 1/\{x_\xi(y_\eta z_\zeta - y_\zeta z_\eta) + y_\xi(x_\zeta z_\eta - x_\eta z_\zeta) + z_\xi(x_\eta y_\zeta - x_\zeta y_\eta)\}.$$

Here U, V and W are contravariant velocities, and J is the Jacobian of the coordinate transformation.

Now the associated boundary conditions will be described. The velocity boundary conditions at the duct wall are

$$u = 0, \quad v = 0, \quad w = 0. \quad (7a)$$

For the temperature boundary conditions at the duct wall, only the curved region is heated and the straight fore- and after-tangents are assumed adiabatic. Thus, the thermal boundary condition for the straight tangents is

$$\partial T/\partial n = 0 \text{ (adiabatic wall)}, \quad (7b)$$

and for the curved region

$$T_w = 1$$

(in the case of constant wall temperature condition) (7c)

or

$$\partial T/\partial n = 0.1(Re\, D^2/S_c)$$

(in the case of constant wall heat flux condition) (7d)

where n denotes the direction normal to duct wall, and S_c the dimensional total surface area of the curved region of the duct. In the process of deriving (7d), it is noted that the nondimensionalization of temperature is in accordance with (3b) (see Akiyama *et al.* [15]). It should also be mentioned that $Pr = 1.0$, and the numerical value of the rise of the nondimensional bulk temperature between the inlet and outlet was set to be 0.2. This particular value of 0.2 was selected in order to facilitate quantitative comparisons of the present results with the numerical data of Akiyama (see the results of run number (1) of Akiyama [15], for $Re = 1000$, $R = 2$, $De = 500$, $Pr = 0.71$). Due to the nondimensionalization schemes adopted in the present paper, the values of the temperatures in the present results are approximately 10 times those of the nondimensional temperatures of ref. [15].

Due to symmetry of the duct geometry, only one half of the duct passage is included in the numerical calculation. The conditions on the duct symmetry plane are

$$w = 0, \quad \frac{\partial u}{\partial z} = 0, \quad \frac{\partial v}{\partial z} = 0, \quad \frac{\partial T}{\partial z} = 0. \quad (7e)$$

The duct inlet velocity was specified as that of fully developed laminar flow in a straight square duct flow, obtainable from the analytic solution [16]. The velocity is normalized by the average inflow velocity u_0. In order to minimize the effect of the inlet and exit boundary conditions on the flow fields in the curved region, the inlet and exit planes are located at sufficiently large distances from the curved region; the inlet plane is located at 10 hydraulic diameters upstream of the curved section, and the exit boundary condition is given at 30 hydraulic diameters downstream, as shown in Fig. 1. The lengths of inlet and outlet tangents taken in this study are larger than those taken by other numerical studies [3, 10, 12].

The inlet boundary conditions, imposed at $10D$ upstream of the curved region, are $u =$ the series solution of fully developed laminar flow in a straight square duct (Ward–Smith [16])

$$v = 0, \quad w = 0, \quad T = 0. \quad (7f)$$

The exit boundary conditions, enforced at $30D$

downstream of the curved region, are given by the Neumann-type conditions [17]

$$\frac{\partial u}{\partial y}=0,\quad \frac{\partial v}{\partial y}=0,\quad \frac{\partial w}{\partial y}=0,\quad \frac{\partial T}{\partial y}=0. \tag{7g}$$

The main task now is to secure a suitable numerical solution technique for the system of partial differential equations (6) in the transformed domain, described by one scalar variable ϕ with the associated boundary conditions (7a)–(7g).

3. NUMERICAL METHOD

The governing equations were solved by using the SIMPLE-C algorithm, which had been documented in refs. [18, 19]. This algorithm upgraded the pressure correction technique of the original SIMPLE algorithm [20]. A hybrid scheme suggested by ref. [20] has been employed to represent the convection and diffusion terms. Iterations were required to attain converged solutions with a prescribed accuracy level (10^{-6} in the present study). The spatial mesh points were $(103\times 25\times 15)$ in the (ξ,η,ζ) computational domain. The mesh was stretched to cluster the grid points near the duct walls. All computations were implemented on a CRAY-2S supercomputer.

Equation (6) is integrated over the control volume $d\xi\, d\eta\, d\zeta$, and it can be cast into a general form of finite difference formulation

$$A_p\phi_p = A_e\phi_e + A_w\phi_w + A_n\phi_n + A_s\phi_s + A_t\phi_t + A_b\phi_b + S_0 \tag{8}$$

where,

$$A_p = A_e + A_w + A_n + A_s + A_t + A_b$$

and A_e, A_w, A_n, A_s, A_t, A_b are the link coefficients, and S_0 the discretized source term. From equations (4) and (8), the finite difference forms of momentum equations can be written as

$$\begin{aligned} A_p^u\hat{u}_p &= \sum_j A_j^u\hat{u}_j + S^u - \hat{P}_x\\ A_p^v\hat{v}_p &= \sum_j A_j^v\hat{v}_j + S^v - \hat{P}_y\\ A_p^w\hat{w}_p &= \sum_j A_j^w\hat{w}_j + S^w - \hat{P}_z. \end{aligned} \tag{9}$$

Using properly guessed values of pressure and velocities, approximate velocity components of $\hat{u}$, $\hat{v}$ and $\hat{w}$ can be obtained from equation (9). To satisfy the continuity equation, the pressure and velocities are corrected by

$$P=\hat{P}+P',\quad u=\hat{u}+u',\quad v=\hat{v}+v',\quad w=\hat{w}+w'. \tag{10}$$

The velocity correction equations are obtained using equations (9) and (10):

$$\begin{aligned} A_p^u u_p' &= \sum_j A_j^u u_j' + S^u - P_x'\\ A_p^v v_p' &= \sum_j A_j^v v_j' + S^v - P_y'\\ A_p^w w_p' &= \sum_j A_j^w w_j' + S^w - P_z'. \end{aligned} \tag{11}$$

In line with the SIMPLE-C algorithm, the above velocity correction equations (11) become

$$u_p' = D^u P_x',\quad v_p' = D^v P_y',\quad w_p' = D^w P_z' \tag{12}$$

where,

$$D^u = -1\Big/\left(A_p - \sum_j A_j^u\right),\quad D^v = -1\Big/\left(A_p - \sum_j A_j^v\right),$$

$$D^w = -1\Big/\left(A_p - \sum_j A_j^w\right).$$

Introducing equations (12) into the continuity equation (1a), the Poisson equation is obtained:

$$(D^uP_x')_x + (D^vP_y')_y + (D^wP_z')_z = \hat{u}_x + \hat{v}_y + \hat{w}_z. \tag{13}$$

After solving equation (13), the corrected velocities and pressure can be found from equations (10) and (12), and these corrected velocities and pressure can be used again as the initial guesses for equation (9). The same procedure is repeated until converged solutions of velocities and pressure are achieved.

The three momentum equations and energy equation are uncoupled in the forced convection heat transfer calculation; therefore, only after the fully converged solutions for velocity fields are in place, the thermal fields are computed.

4. RESULTS AND DISCUSSION

Table 1 summarizes the parameter values for the runs in the present computations. In order to systematically assess the effect of the Reynolds number, five different values of Re were chosen. As stipulated in equations (3a) and (3b), for each run, two cases of the thermal boundary conditions at the duct wall were used. The Prandtl number was set $Pr = 1.0$. The case of $Re = 790$ serves as a benchmark test; the numerical results can be explicitly checked against the existing data in the literature [3, 4, 10–13] which were made for this particular value of Re.

In the ensuing sections, eminent features of flow and

Table 1. Parameter values for the computations

Re	R	De
50	2.3	23
500	2.3	233
790	2.3	368
	4.6	260
1000	2.3	466
2000	2.3	933

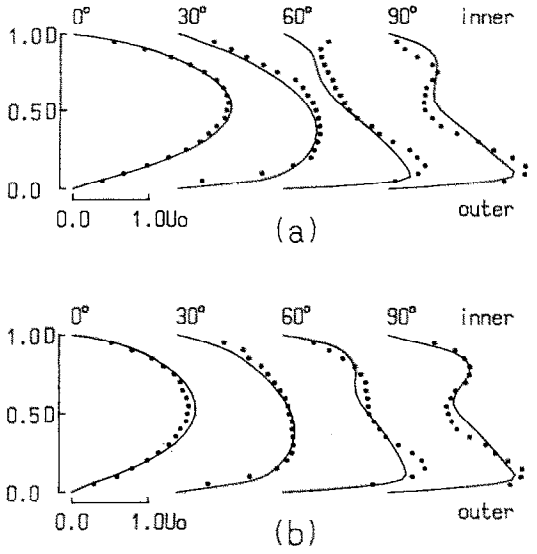

FIG. 2. Development of main stream velocity ($Re = 790$, $R = 2.3$). —— present results, ○ experiment (ref. [3]). (a) Symmetry plane; (b) plane at $0.25D$ from the side wall.

heat transfer will be discussed for two representative cases, $Re = 50$ and $Re = 790$; these two characterize the flow properties in the low- and high-Reynolds number regimes.

4.1. *Flow and pressure drop*

We shall first briefly review the velocity patterns. The flow structures in a curved duct at a relatively high Re have been described previously [3, 4, 10, 12]; we shall recapitulate the highlights only.

Figure 2 exemplifies the developing mainstream flows in the curved region at $Re = 790$. The mainstream velocity becomes larger near the outer wall as the flow moves downstream. The variations in the z-direction, which denote the three-dimensionality, are also captured well by the present computations. Figure 2 is shown to appraise the reliability and accuracy of the present numerical simulations by repeating parallel computations to the experimental measurements of ref. [3]; the agreement, as demonstrated in Fig. 2, is satisfactory.

Figure 3 exhibits both the mainstream and secondary flows for a low-Re regime (Fig. 3(a) for $Re = 50$) and for a high-Re regime (Fig. 3(b) for $Re = 790$). As ascertained, independent flow data are available [3, 4] for $Re = 790$, and the general flow patterns based on the present numerical results are consistent with these preceding observations. It is noted that, in the high-Re regime, a small area of flow reversal is present in the corner between the outer and side walls near the entrance region of the curved duct (see Fig. 3(b) at $\theta = 0°$ and $\theta = 30°$). This is due to an appreciable adverse pressure gradient arising from

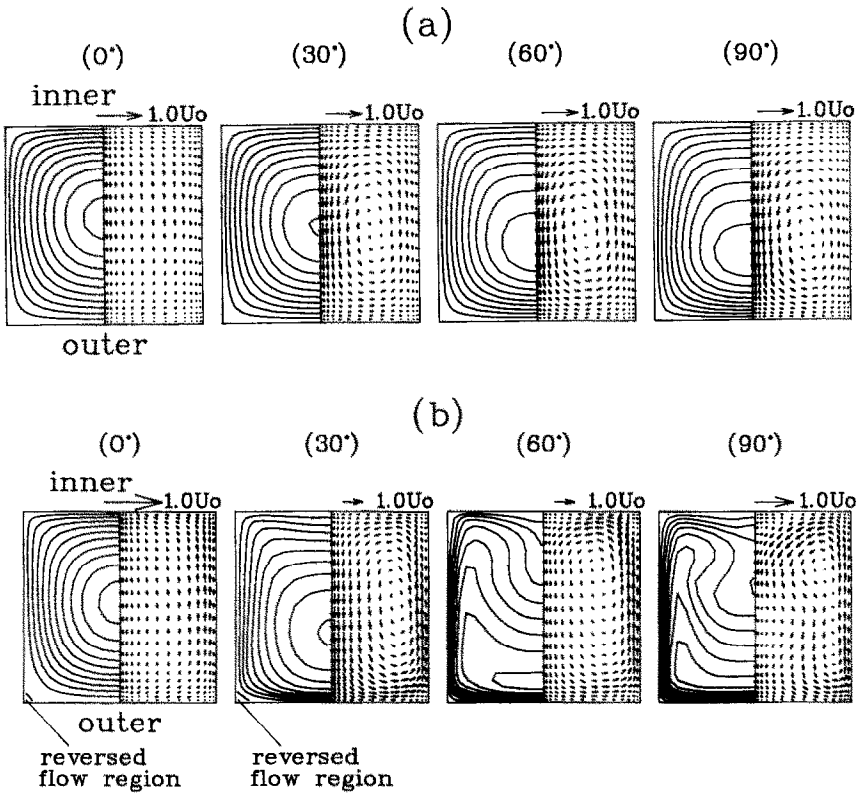

FIG. 3. Iso-velocity lines of mainstream (left half plane) and secondary flow patterns (right half plane). The values of iso-velocity contour lines, are from outer to inner wall, 0.2, 0.4, 0.6, 0.8, 1.0, 1.2, 1.4, 1.6 and 1.8. (a) $Re = 50$, $R = 2.3$; (b) $Re = 790$, $R = 2.3$.

substantial curvature effects. Further details of the mainstream flow near the curved walls are depicted in Fig. 4. As pointed out in Fig. 3(b), the presence of a reverse flow zone in the vicinity of the corner between the outer and side walls in the range $0° \leqslant \theta \leqslant 30°$ is discernible in Fig. 4(b). The direction of the flow near the side wall is consistent with the flow visualization of ref. [4]. However, as manifested in Figs. 3(a) and 4(a), when Re is low, the flow reversal is not conspicuous; in the low-Re regime, the adverse pressure gradient is not sufficient to cause the reverse flow. The observation of ref. [3] had suggested that the reverse flow zone exists in a duct when the Dean number $De > 125$. The elaborate numerical computational results of this study are qualitatively supportive of this experimental finding. Figures 3 and 4 clearly recapture the well-documented general flow character; at high Re, the secondary flows are more vigorous, and the position of the maximum mainstream velocity moves toward the outer and side walls. The behavior of secondary flows at $\theta = 0°$ merits some mention. The present numerical results indicate that at $\theta = 0°$, the secondary flows are predominantly directed toward the inner wall in both Figs. 3(a) and (b). This is in conformity with the recent experimental and numerical studies of refs. [14, 21]. This may be attributed to the apparent imbalance of radial pressure gradient and the centrifugal force. Near the inlet section of the curved duct, a positive radial pressure gradient already exists, but the centrifugal force, which drives radially outward flow, has not built up yet. The intensification of the secondary flow, as the curve angle θ increases, is discernible in Figs. 3(a) and (b).

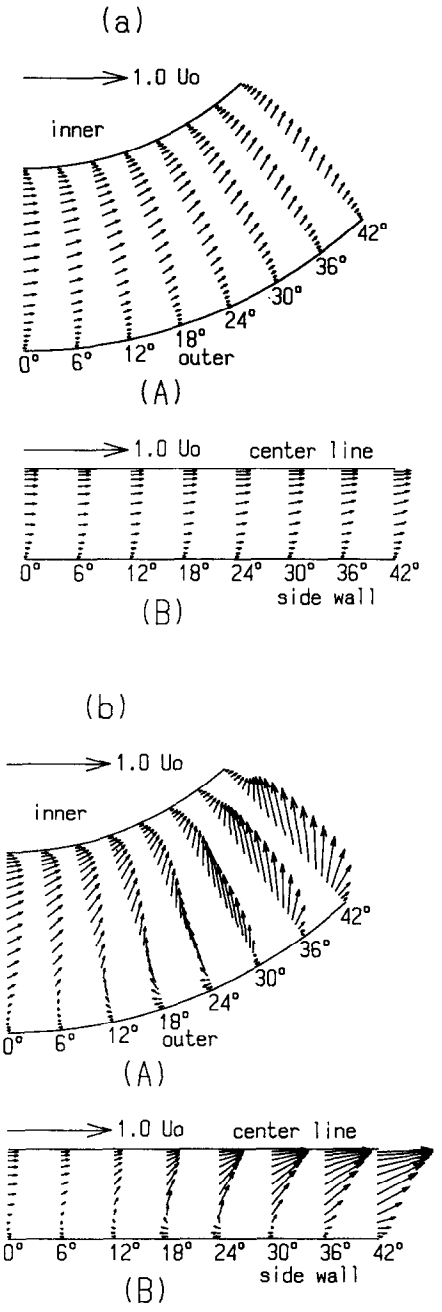

FIG. 4. Mainstream velocity vectors. (A) On the plane located at $0.0136D$ from the side wall; (B) on the plane located at $0.0147D$ from the outer wall. (a) $Re = 50$, $R = 2.3$; (b) $Re = 790$, $R = 2.3$.

The pressure distributions, as depicted by average pressure coefficients $\overline{C_p}$, are plotted in Fig. 5. In Fig. 5 the cross-sectional average pressure coefficient, $\overline{C_p}$, at a given curve angle θ, is defined by

$$\overline{C_p} = \int C_p \, dA \Big/ \int dA,$$

where dA is the infinitesimal cross-sectional area perpendicular to the axial direction. Also, at the inner or outer wall, the average pressure coefficient, $\overline{C_{p_w}}$, at a given curve angle θ, is defined by

$$\overline{C_{p_w}} = \frac{1}{L} \int C_p \, dL,$$

where L denotes the local wall width concerned. In general, pressure is high (low) near the outer (inner) wall, a well-known phenomenon in a curved duct. However, this radial pressure gradient varies substantially with the curve angle. It is noticeable that in the high-Re regime (e.g. see Fig. 5(b) at $Re = 790$), the unfavorable pressure gradient in the mainstream direction is substantial on the outer wall between $\theta \cong 0°$ and $\theta \cong 45°$. This gives rise to the reversal of mainstream flow between $\theta \cong 0°$ and $\theta \cong 35°$, as demonstrated in Figs. 3(b) and 4(b). The computed result of cross-sectional average pressure coefficient, $\overline{C_p}$, in Fig. 5(b) is in good agreement with the data of ref. [3].

4.2. *Heat transfer*

We now turn to the thermal field and associated heat transfer. As remarked earlier, the developing heat transfer in a duct with strong curvature has not been addressed in sufficient detail in the literature. It is noted that ref. [11] produced temperature distri-

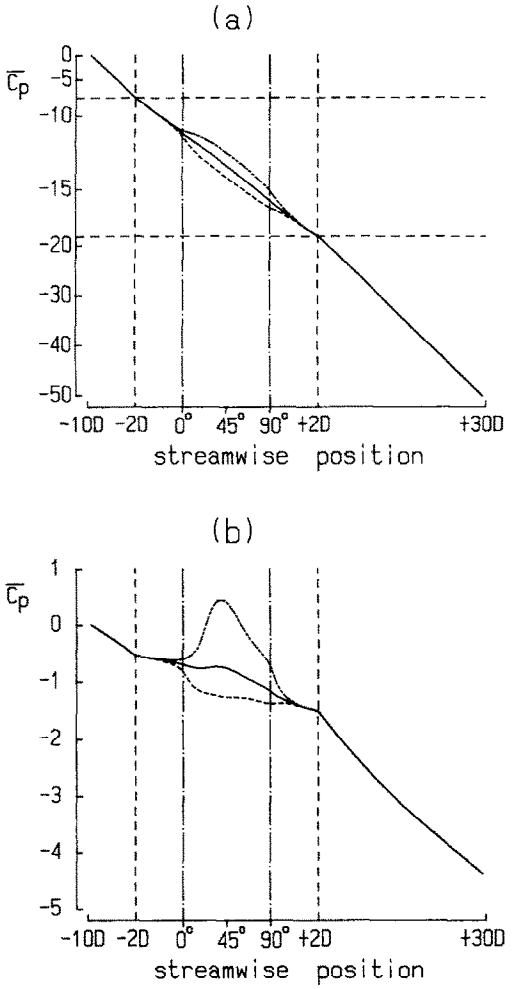

FIG. 5. Axial variations of average pressure coefficients $\overline{C_p}$. (The abscissa and ordinate for the bend are enlarged for clarity.) —— $\overline{C_p}$, cross-sectional average, --- $\overline{C_{p_w}}$ at the inner wall, —·— $\overline{C_{p_w}}$ at the outer wall. (a) $Re = 50$, $R = 2.3$; (b) $Re = 790$, $R = 2.3$.

butions by performing three-dimensional elliptic type calculations using a rather coarse mesh. These computations were about a single Reynolds number $Re = 790$, and the constant wall temperature condition was prescribed. A careful literature survey has revealed no other apparent published information on this particular aspect of heat transfer problems.

First, axial variations of the thermal fields are scrutinized. It is advantageous to define a bulk temperature T_b inside the duct as

$$T_b = \int UT\,dA \Big/ \int U\,dA,$$

where U is the axial velocity, dA the infinitesimal cross-sectional area perpendicular to the axial direction. In the present problem formulation, only the curved portion of the duct is exposed to external thermal forcing (e.g. constant wall temperature or constant heat flux through the wall), and the straight tangents are insulated. Consequently, it follows that the variation in T_b is expected only in the curved portion.

Figure 6 illustrates the axial variations of T_b. Under the condition of constant heat flux at the wall, the variation of T_b is approximately linear in the axial direction, as can be easily anticipated. However, for the case of constant wall temperature condition at the wall, some comments are in order. Figure 6(c) indicates that, in the low-Re regime ($Re = 50$), the rate of increase of T_b is rapid near and immediately after the inlet of the curved duct. In this low-Re regime, the influence of the secondary flow is meager (see Fig. 3(a)); the heat transport characteristics are qualitatively akin to those inside a straight duct. On the other hand, in the high-Re regime (see Fig. 6(d) for $Re = 790$), the rate of change of T_b is fairly uniform throughout the entire curved portion of the duct. In this case, the secondary flow is intense, and the overall heat transfer is effectuated by axial as well as secondary flow. It is worth noting in Fig. 6 that, although only the curved portion is exposed to external thermal forcings, T_b starts to be affected a little ahead of the curved inlet ($\theta = 0°$). This manifests the elliptic nature of the present computations. An analogous feature was discernible in the plots of the pressure fields, as shown in Fig. 5. The computational results of ref. [15] about a curved pipe disclosed a similar trend in the axial variation of T_b.

The three-dimensional structures of thermal fields in the developing region are exhibited in Fig. 7. It is obvious that the isotherm contours in the cross-sectional views resemble the iso-velocity contours of the mainstream, as depicted in Fig. 3. This was observed also previously by Yee *et al.* [11]. In particular, in the high-Re regime (see Figs. 7(b) and (d) for $Re = 790$), the isotherm contours are crowded near the outer and side walls, especially at large values of θ; these are characteristic of the mainstream velocity contours. As asserted earlier, the impact of secondary flow on the convective transport is substantial, and, consequently, the maximum of the axial flow tends to be shifted toward the outer and side walls. At very small values of θ, the axial flow is larger near the inner wall than the outer wall; therefore, convective heat transfer is more effective near the inner wall region. However, as θ increases, the axial flow intensifies near the outer wall owing to the centrifugal force generated in the curved passage. This brings about enhanced convective heat transfer activities near the outer wall region.

An interesting feature of the thermal field pattern may be seen near the corner of the outer and side walls in the high-Re regime near $\theta = 0°$ (see Fig. 7(b)). Notice that the local temperature near this corner reaches a high value, although the bulk temperature at the inlet of the curved duct ($\theta = 0°$) is very low. The occurrence of a localized area of high temperature may be identified as an extreme reduction of convective heat transport in this region. This is attributed to the presence of the zone of flow reversal, which

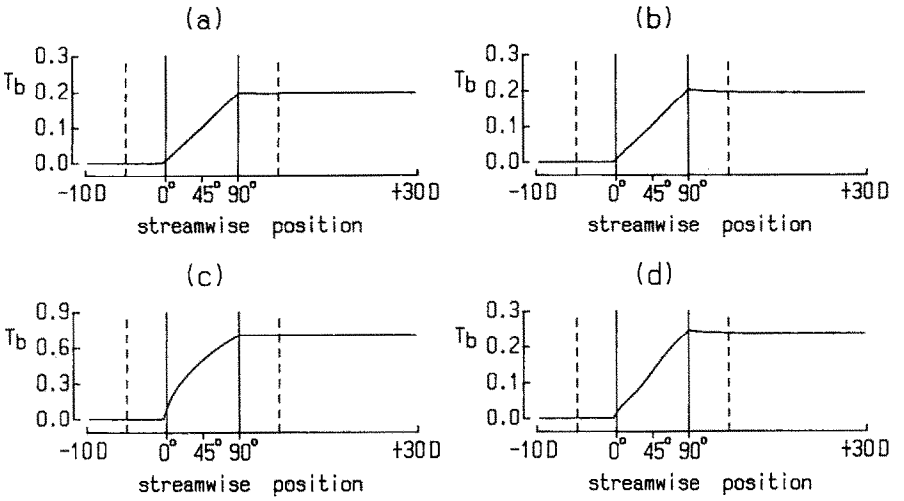

FIG. 6. Axial variations of bulk temperature T_b. (The abscissa for the bend are enlarged for clarity.) (a) $Re = 50$, $R = 2.3$; constant wall heat flux boundary condition. (b) $Re = 790$, $R = 2.3$; constant wall heat flux boundary condition. (c) $Re = 50$, $R = 2.3$; constant wall temperature boundary condition. (d) $Re = 790$, $R = 2.3$; constant wall temperature boundary condition.

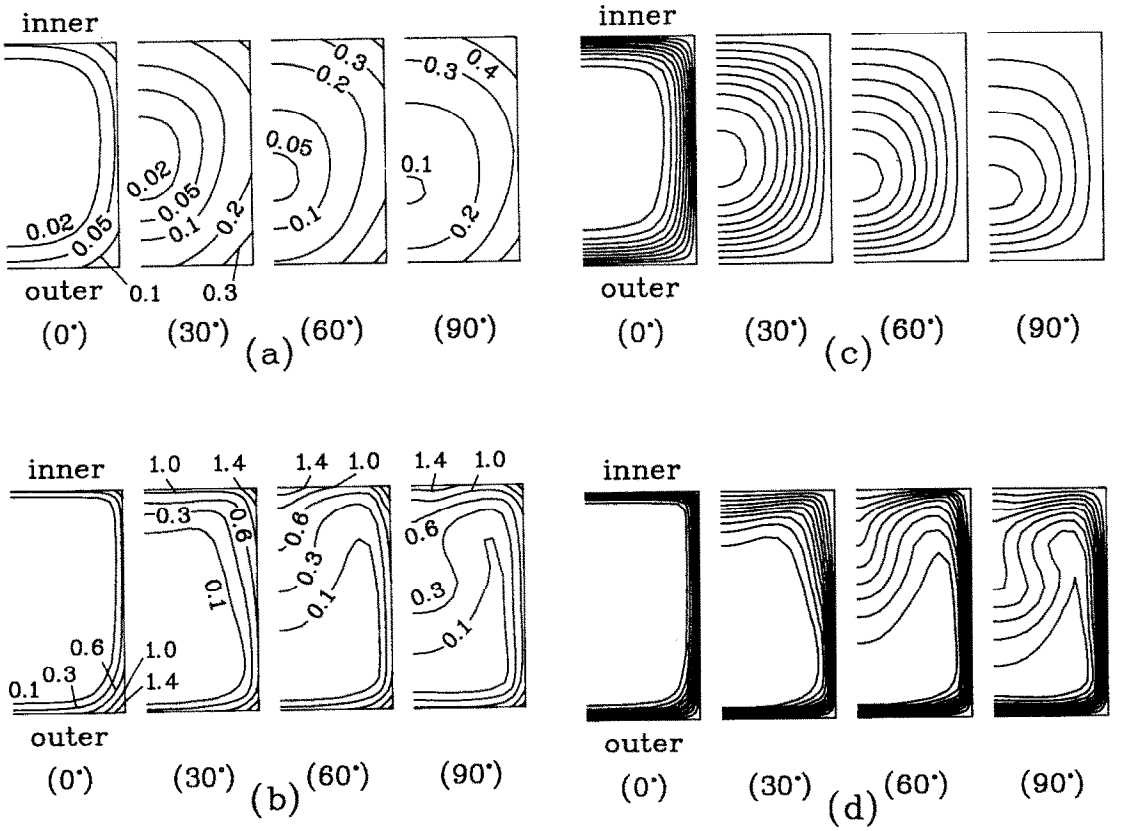

FIG. 7. Plots of isotherms in the cross-sectional planes. (a) $Re = 50$, $R = 2.3$; constant wall heat flux boundary condition. (b) $Re = 790$, $R = 2.3$; constant wall heat flux boundary condition. (c) $Re = 50$, $R = 2.3$; constant wall temperature boundary condition. The values of isotherm contours, are from outer to inner walls, 0.9, 0.8, 0.7, 0.6, 0.5, 0.4, 0.3, 0.2 and 0.1. (d) $Re = 790$, $R = 2.3$; constant wall temperature boundary condition. The values of isotherm contours, are from outer to inner walls, 0.9, 0.8, 0.7, 0.6, 0.5, 0.4, 0.3, 0.2 and 0.1.

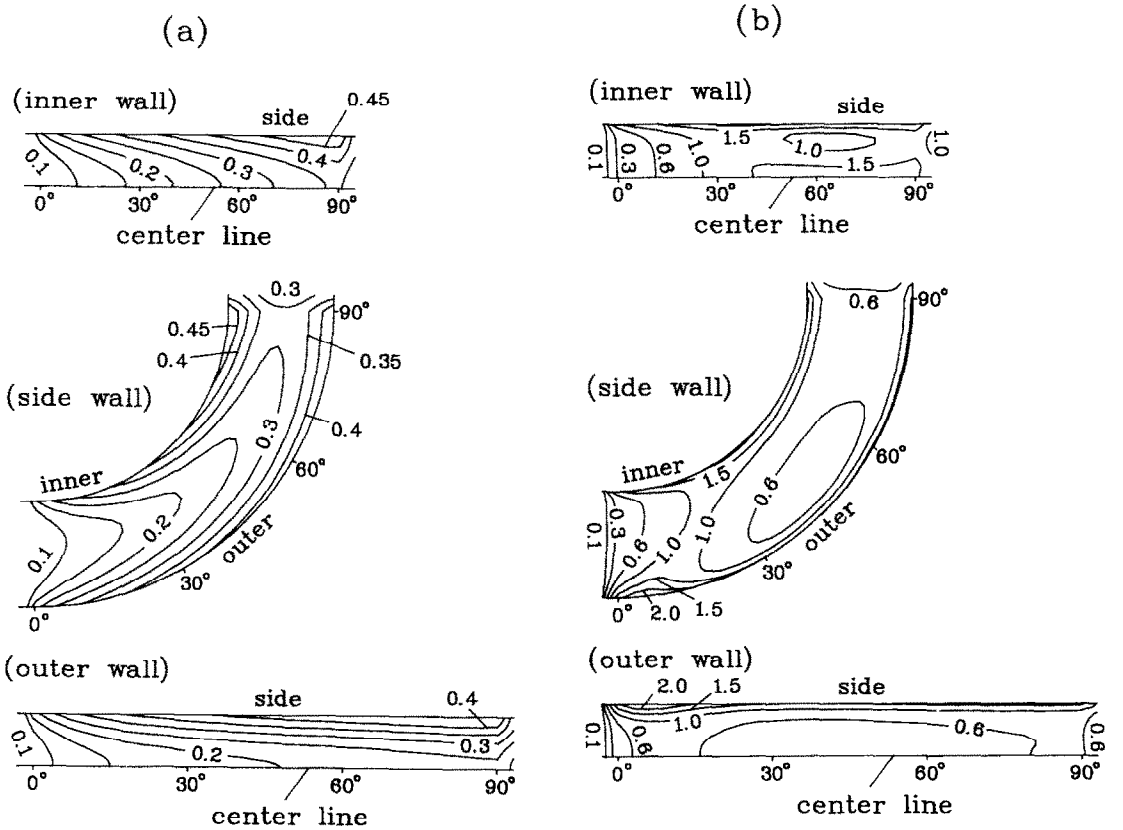

FIG. 8. Surface temperature distributions (constant wall heat flux boundary condition). (a) $Re = 50$, $R = 2.3$; (b) $Re = 790$, $R = 2.3$.

was discussed earlier (see Figs. 3(b) and 4(b)). The numerical study of ref. [15] for a 90° curved pipe also disclosed a qualitatively similar trend of having a localized high-temperature region near the outer wall in the inlet plane. Due to the geometrical difference between ref. [15] and the present study, no direct and more quantitative comparisons are tenable between these two sets of results.

The constant-flux thermal boundary condition imposed on the duct wall may be viewed as an approximation to certain realistic industrial systems. In these situations, accurate determination of the duct surface temperature distribution is a meaningful task. Examples may be found in various types of precision heat exchangers, which include a large number of curved ducts. Figure 8 exhibits isotherm contour plots on the surfaces of the duct. At a given cross-sectional plane, the local temperature is, in general, higher near the corner regions than in the interior; convective activities are weaker in the corner regions due to the existence of slower-moving particles. The presence or absence of the corner region makes the principal difference between the case of a curved duct and a curved pipe [15]. As succinctly demonstrated in Fig. 8(a), in the low-Re regime, the region of highest temperature is located near the corner of the inner and side walls at a small distance prior to $\theta = 90°$. The axial velocity is minimum at this location. On the contrary, in the high-Re regime (see Fig. 8(b)), the highest temperature is found near the corner of the outer and side walls somewhere between $\theta = 0°$ and $\theta = 15°$. As stressed previously, this region corresponds to the zone of flow reversal (see Figs. 3(b) and 4(b)). It is also of interest to observe in Fig. 8(b) that the overall temperature distributions in the corner areas between the inner and side walls tend to be high. Figure 8(b) also shows a region of relatively high temperatures in the vicinity of the symmetry line on the inner wall between $\theta \approx 40°$ and $\theta \approx 90°$. The presence of this region signifies the role of secondary flow, which scoops heat from the outer wall region and transports it to near the inner wall in the middle and upper parts of the curved duct ($\theta \approx 40°$ to $\theta \approx 90°$).

The Nusselt number is a key parameter which can be acquired by analyzing the computed thermal field. For the present three-dimensional flow data, it is advantageous to introduce suitably-averaged Nusselt numbers. The peripherally-averaged Nusselt number, $\overline{Nu}_p$, at a given curve angle θ, is defined as

$$\overline{Nu}_p = -\frac{1}{L_p}\int\left(\frac{1}{T_w - T_b}\right)\left(\frac{\partial T}{\partial n}\right)_{wall} dL_p,$$

in which L_p represents the peripheral length and n the

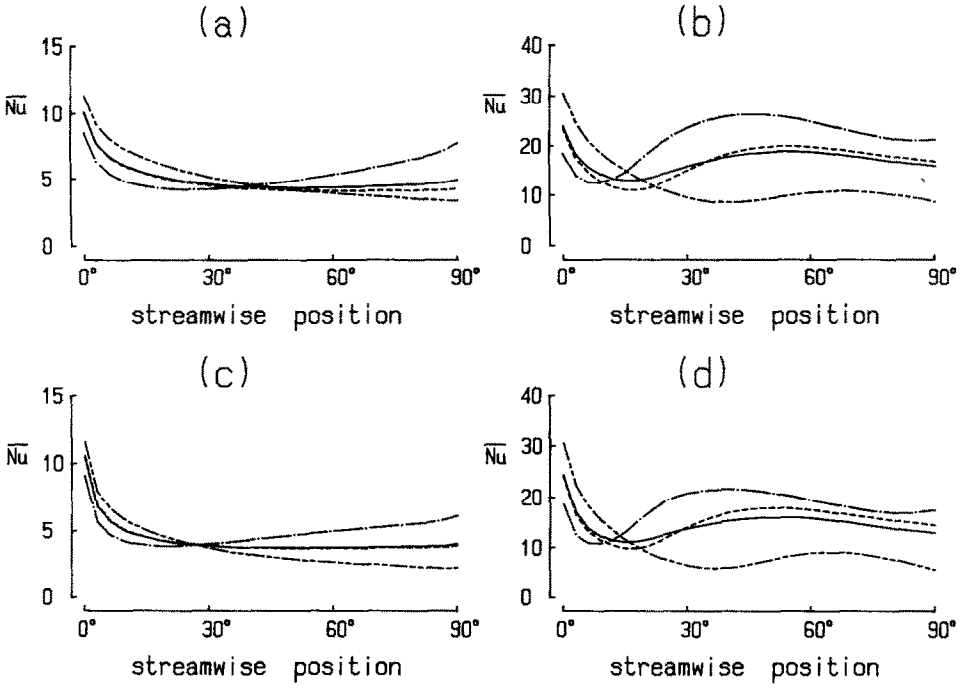

FIG. 9. Axial variations of average Nusselt numbers. ——— peripheral average; --- side wall average; -·-·- outer wall average; ·····- inner wall average. (a) $Re = 50$, $R = 2.3$; constant wall heat flux boundary condition. (b) $Re = 790$, $R = 2.3$; constant wall heat flux boundary condition. (c) $Re = 50$, $R = 2.3$; constant wall temperature boundary condition. (d) $Re = 790$, $R = 2.3$; constant wall temperature boundary condition.

direction normal to the duct wall. In a similar manner, the plane-averaged Nusselt number, $\overline{Nu}$, at a given curve angle θ, for the component wall of the duct, i.e., the inner, outer, or side wall, is defined as

$$\overline{Nu} = -\frac{1}{L}\int\left(\frac{1}{T_w - T_b}\right)\left(\frac{\partial T}{\partial n}\right)_{wall} dL,$$

where L denotes the local width of the wall concerned.

Figure 9 illustrates the above-defined Nusselt numbers. In the first, when the Reynolds number is low (see Figs. 9(a) and (c)), the secondary flow is weak and convective heat transfer is dominated by the axial flow. On the surface of outer wall, the Nusselt number decreases mildly with axial distance from the duct inlet ($\theta = 0°$) to intermediate values of the curve angle ($\theta \cong 20$–$30°$). After passing through a minimum, $\overline{Nu}$ increases gradually in the downstream areas up to the duct exit ($\theta = 90°$). The Nusselt number variations on the surfaces of other walls are similar to those of a straight duct flow. On the other hand, in the high-Re regime (see Figs. 9(b) and (d)), a substantially different picture emerges. The secondary flows and the distortion of the axial flows toward outer and side walls play a significant role, and the heat transfer properties show considerable axial variations accordingly. In the inlet region of the curved duct, the peripherally-averaged Nusselt number, $\overline{Nu}_p$, initially decreases with the axial distance until reaching a minimum around $\theta = 15°$. In this inlet region, the secondary flow has not developed yet to a sufficient strength. At intermediate and large curve angles ($\theta \gtrsim 15°$), secondary flows are substantial in magnitude, and, as a result of these secondary flows, heat transfer is enhanced. Figure 9 reaffirms the anticipation that the intensification of the global heat transfer is noticeable in the high-Re regime (compare the magnitudes of the ordinates in Fig. 9). Perusal of Figs. 9(b) and (d) recaptures the earlier assertion that, in the inlet region, $\overline{Nu}$ is higher on the inner wall than on the outer wall, but after $\theta \approx 15°$, the trend is reversed. It is also interesting to gauge the difference in $\overline{Nu}$ between the inner and outer walls; the difference is largest near $\theta = 40°$. The axial variations of $\overline{Nu}$ on the side wall and of $\overline{Nu}_p$ are comparatively mild, and they are qualitatively similar to $\overline{Nu}$ on the outer wall.

In an effort to portray the local heat transfer characteristics, the peripheral profiles of the local Nu in the developing flow region are mapped in Fig. 10. The local Nu is evaluated,

$$Nu = -\frac{1}{T_w - T_b}\left(\frac{\partial T}{\partial n}\right)_{wall}.$$

In general, peripheral variations of Nu are more pronounced at high Reynolds numbers, as expected. In the low-Re regime (see Figs. 10(a) and (c)), the profiles of local Nu on the inner and outer walls bulge toward the symmetry plane. On the side wall, the local Nu

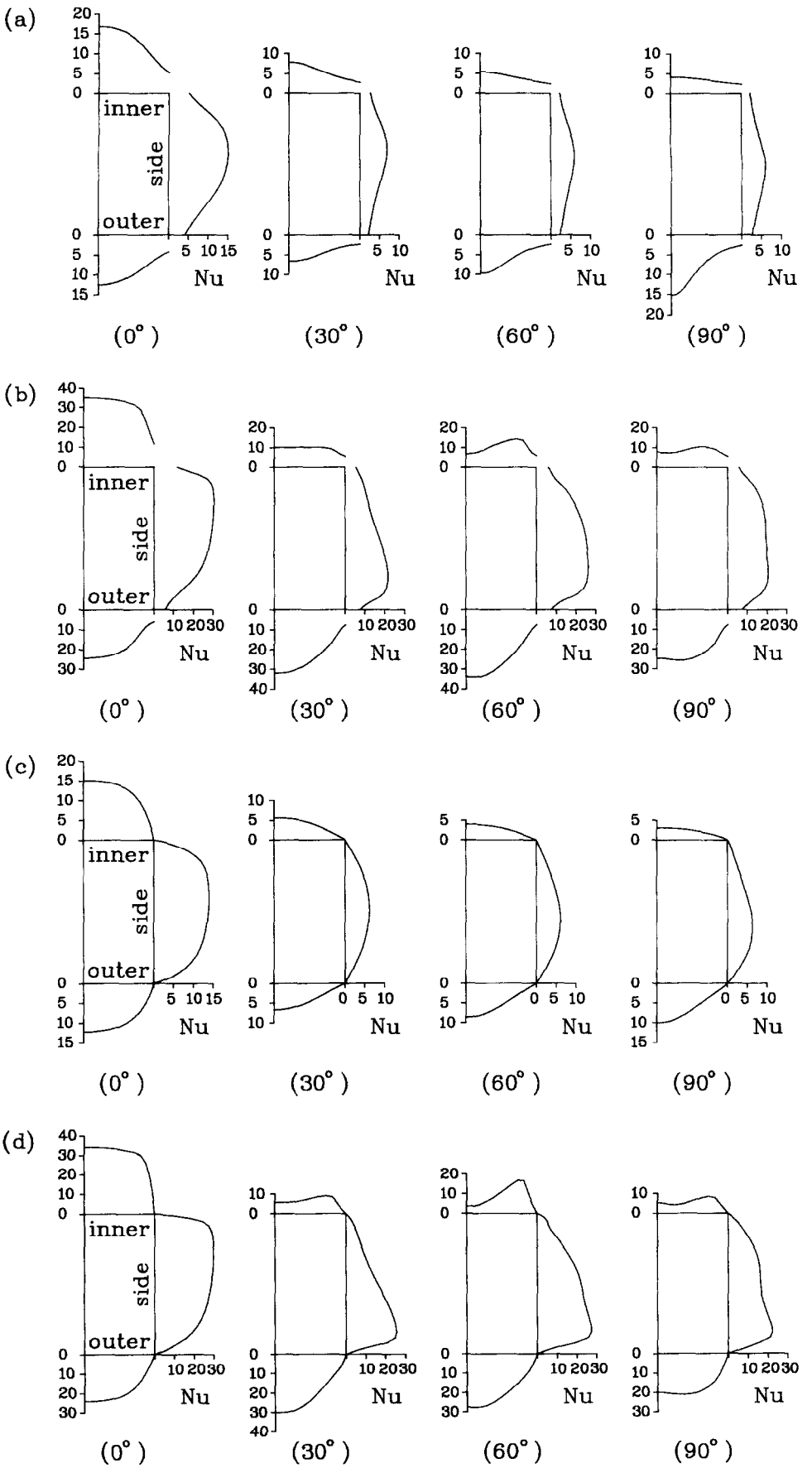

FIG. 10. Profiles of local Nusselt numbers on the surfaces. (a) $Re = 50$, $R = 2.3$; constant wall heat flux boundary condition. (b) $Re = 790$, $R = 2.3$; constant wall heat flux boundary condition. (c) $Re = 50$, $R = 2.3$; constant wall temperature boundary condition. (d) $Re = 790$, $R = 2.3$; constant wall temperature boundary condition.

tends to be large near $\theta = 0°$ and tends to decrease slightly with the downstream axial distance.

The local *Nu* maps display more complex patterns in the high-*Re* regime (see Figs. 10(b) and (d)). The overall shapes of these plots are consistent with the physical descriptions of the flow and thermal fields that were offered earlier. The local-*Nu* profiles contained in Fig. 10(d) at $\theta = 90°$ are in close agreement with the results of ref. [13]; no precision comparisons were attempted since the data of ref. [13] were given for the plane at $\theta = 87°$ only.

5. CONCLUSIONS

Extensive and systematically-organized numerical results of flow and heat transfer properties have been obtained for a developing flow in a 90°-curved square duct. The fully elliptic three-dimensional Navier–Stokes equations have been solved.

The computed flow field is consistent with the available data in the literature. The flow characteristics in the low- and high-*Re* regimes are depicted in detail. At high *Re*, a zone of reverse flow is present near the corner of outer and side walls; the adverse pressure gradient is appreciable in this zone.

Details of the temperature field and the associated heat transfer were analyzed and appropriate physical explanations were offered. In the high-*Re* regime, the axial variations of the Nusselt numbers, both averaged and local, exhibit interesting behavior. In the duct inlet region, convective heat transfer is higher on the inner wall than on the outer wall. However, at intermediate and far downstream locations, heat transfer is more effective on the outer wall. It is important to note that heat transfer is much reduced in the zone of reverse flow, which occurs near the inlet outer wall–side wall corner area.

Acknowledgements—This work was supported in part by research grants from the Korean Ministry of Science and Technology and from the Advanced Fluids Engineering Research Center (AFERC) of Pohang Institute of Science and Technology, Pohang, Korea.

REFERENCES

1. K. C. Cheng, Ran-Chau Lin and Jenn-Wuu Ou, Fully developed laminar flow in curved rectangular channels, *J. Fluids Engng* **98,** 41–48 (1976).
2. K. N. Ghia, U. Ghia and C. T. Shin, Study of fully developed incompressible flow in curved ducts, using a multi-grid technique, *J. Fluids Engng* **109,** 226–236 (1987).
3. J. A. C. Humphrey, A. M. K. Taylor and J. H. Whitelaw, Laminar flow in a square duct of strong curvature, *J. Fluid Mech.* **83,** 509–527 (1977).
4. A. M. K. P. Taylor, J. H. Whitelaw and M. Yianneskis, Curved ducts with strong secondary motion: velocity measurements of developing laminar and turbulent flow, *J. Fluids Engng* **104,** 350–359 (1982).
5. K. C. Cheng and M. Akiyama, Laminar forced convection heat transfer in curved rectangular channels, *Int. J. Heat Mass Transfer* **13,** 471–490 (1970).
6. Y. Mory, Y. Uchida and T. Ukon, Forced convective heat transfer in a curved channel with a square cross section, *Int. J. Heat Mass Transfer* **14,** 1787–1805 (1971).
7. K. C. Cheng, Ran-Chau Lin and Jenn-Wuu Ou, Graetz problem in curved rectangular channels with convective boundary condition—the effect of secondary flow on liquid solidification-free zone, *Int. J. Heat Mass Transfer* **18,** 996–999 (1975).
8. D. E. Metzer and D. E. Larson, Use of melting point surface coatings for local convection heat transfer measurements in rectangular channel flows with 90-deg turns, *J. Heat Transfer* **108,** 48–54 (1986).
9. K. N. Ghia and J. S. Sokhey, Laminar incompressible viscous flow in curved ducts of rectangular cross-sections, *J. Fluids Engng* **99,** 640–648 (1977).
10. C. M. Rhie, A three-dimensional passage flow analysis method aimed at centrifugal impellers, *Comput. Fluids* **13,** 443–460 (1985).
11. G. Yee, R. Chilukuri and J. A. C. Humphrey, Developing flow and heat transfer in strongly curved ducts of rectangular cross section, *J. Heat Transfer* **102,** 285–291 (1980).
12. S. Pratap Vanka, Block-implicit calculations of three-dimensional laminar flow in strongly curved ducts, *AIAA J.* **23,** 1989–1991 (1985).
13. R. Chilukuri and J. A. C. Humphrey, Numerical computation of buoyancy-induced recirculation in curved square duct laminar flow, *Int. J. Heat Mass Transfer* **24,** 305–314 (1981).
14. T. Kajishima, Y. Miyake and T. Inaba, Numerical simulation of laminar flow in curved ducts of a rectangular cross-section, *Trans. J.S.M.E.* **54,** 503, 1594–1601 (1988) (in Japanese).
15. M. Akiyama, H. Sugiyama, M. Saitoh, I. Nishiwaki, T. Murakoshi and K. C. Cheng, Numerical computation of convective heat transfer in the bend tube flow by time-dependent three-dimensional parabolic equations, *Trans. J.S.M.E.* **54,** 507, 3219–3226 (1988) (in Japanese).
16. A. J. Ward-Smith, *Internal Fluid Flow: The Fluid Dynamics of Flow in Pipes and Ducts*, p. 18. Clarendon Press, Oxford (1980).
17. K. A. Hoffman, *Computational Fluid Dynamics for Engineers*, p. 13. EES Austin, Texas (1989).
18. J. P. Van Doorman and G. D. Raithby, Enhancements of the SIMPLE method for predicting incompressible fluid flows, *Numer. Heat Transfer* **7,** 147–163 (1984).
19. B. R. Latimer and A. Pollard, Comparison of pressure–velocity coupling solution algorithms, *Numer. Heat Transfer* **8,** 635–652 (1985).
20. S. V. Patankar, *Numerical Heat Transfer and Fluid Flow*. McGraw-Hill, New York (1980).
21. S. Sugiyama, T. Aoi, M. Yamamoto and N. Narisawa, Flows in a curved rectangular channel, *Trans. J.S.M.E.* **55,** 514, 1571–1576 (1989) (in Japanese).

TRANSFERT THERMIQUE CONVECTIF DANS LA REGION D'ETABLISSEMENT D'ECOULEMENT DANS UN CANAL QUARRE A FORTE COURBURE

Résumé—On étudie numériquement les caractéristiques de vitesse et de convection thermique dans un écoulement laminaire dans un conduit carré courbé à 90°, avec parties rectilignes à l'entrée et à la sortie. Les équations elliptiques, tridimensionnelles, permanentes de fluide incompressible selon Navier–Stokes sont résolues numériquement sur des larges domaines de nombre de Reynolds *Re* (et de Dean en correspondance). Un système de coordonnées lié au corps est utilisé. On adopte deux conditions aux limites thermiques: température pariétale constante, densité de flux constant. Les résultats numériques sont cohérents avec les données disponibles sur le champ d'écoulement. Des détails sur le champ de température sont donnés ainsi que sur le nombre de Nusselt dans la région courbe. Au voisinage de l'entrée de la région courbe, le transfert thermique est plus grand sur la paroi interne à cause d'écoulements locaux accélérés près d'elle. Néanmoins, plus en aval, le transfert est plus grand sur la paroi extérieure du fait de la force centrifuge. Quand le nombre de Reynolds augmente, une région de renversement d'écoulement apparaît dans le coin entre les parois externes et latérales près de l'entrée du coude. Le transfert thermique est diminué dans cette région. Les résultats illustrent clairement les variations du nombre de Reynolds à la fois sur la périphérie et dans le sens de l'écoulement principal.

KONVEKTIVER WÄRMEÜBERGANG IN DER EINLAUFZONE EINES QUADRATISCHEN KANALS MIT EINER STARKEN KRÜMMUNG

Zusammenfassung—Das Verhalten von Geschwindigkeit und konvektivem Wärmeübergang bei laminarer Strömung in der Einlaufzone eines quadratischen Kanals mit einer 90°-Krümmung wird umfassend numerisch untersucht. An den Kanal sind gerade Einlaß- und Auslaßkanäle angeschlossen. Die vorständigen elliptischen dreidimensionalen, stationären Navier–Stokes Gleichungen für inkompressible Strömung werden numerisch in einem weiten Bereich der Reynolds-Zahl *Re* (und der korrespondierenden Dean-Zahl) gelöst. Dabei wird ein körperangepaßtes Koordinatensystem verwendet. Im Bereich der Krümmung werden zwei thermische Randbedingungen angenommen: konstante Wandtemperatur und konstante Wärmestromdichte. Die numerischen Ergebnisse sind mit verfügbaren Daten für das Strömungsfeld konsistent. Die Einzelheiten des Temperaturfeldes, sowie die Nusselt-Zahl in der gekrümmten Region werden dargestellt. Der Einfluß der Reynolds-Zahl auf den lokalen Wärmeübergang an verschiedenen Stellen des Strömungsfeldes wird untersucht. Die Übereinstimmung der thermischen Randbedingungen im Bereich der Krümmung wird geprüft. In der Umgebung des Eingangs der gekrümmten Region ist der Wärmeübergang an der inneren Wand aufgrund von lokalen Beschleunigungsströmungen stärker. Der Wärmeübergang wird jedoch weiter stromabwärts an der äußeren Wand intensiver, da das Maximum des Hauptstroms durch die Zentrifugalkraft zur äußeren Wand verschoben wird. Mit zunehmender Reynolds-Zahl erscheint in der Eckregion zwischen den äußeren und den Seitenwänden in der Nähe des Eingangs zur Krümmung ein Gebiet der Rückströmung. Der Wärmeübergang in dieser Gegend ist vermindert. Die vorliegenden berechneten Ergebnisse zeigen klar die Veränderungen der Nusselt-Zahl in Umfangs- und in Strömungsrichtung.

КОНВЕКТИВНЫЙ ТЕПЛОПЕРЕНОС НА УЧАСТКЕ РАЗВИВАЮЩЕГОСЯ ТЕЧЕНИЯ В СИЛЬНО ИЗОГНУТОМ КАНАЛЕ КВАДРАТНОГО СЕЧЕНИЯ

Аннотация—Численно исследуются скорость и характеристики конвективного теплопереноса при развивающемся ламинарном течении в канале квадратного сечения с изгибом в 90°. К входу и выходу из канала примыкают по касательной прямые участки. Численно решаются полностью эллиптические трехмерные стационарные уравнения Навье–Стокса для несжимаемой жидкости в широких интервалах изменения числа Рейнольдса *Re* (и соответствующего числа Дина). Используется система координат, связанная с обтекаемым телом. На изгибе приняты два вида тепловых граничных условий: с постоянной температурой стенки и с постоянным тепловым потоком на стенке. Численные результаты согласуются с имеющимися данными для поля течения. Представлены характеристики температурного поля и число Нуссельта на участке изгиба. Исследуется вияние значения *Re* на локальный теплоперенос в различных областях поля течения. Рассматривается также влияние теплового граничного условия на изгибе. В окрестности входа в участок изгиба теплоперенос более интеисивен на внутренней стенке из-за наличия ускоряющихся течений. Однако с расстоянием вниз по потоку теплоперенос происходит интенсивней на внешней стенке, поскольку максимум основного потока смещается к внешней и боковой стенкам под действием центробежных сил. По мере увеличения числа Рейнольдса в угловой области между внешней и боковой стенками у входа в изгиб возникает участок обратного течения. Полученные результаты расчетов наглядно показывают изменения чисел Нуссельта как на периферии, так и в направлении течения.